

Chemical Science

Volume 15
Number 41
7 November 2024
Pages 16807–17258

rsc.li/chemical-science



ISSN 2041-6539

EDGE ARTICLE

Matthew J. Fuchter, Xiaohong Zhang, Eli Zysman-Colman *et al.*
Helically chiral multiresonant thermally activated delayed
fluorescent emitters and their use in hyperfluorescent
organic light-emitting diodes

Cite this: *Chem. Sci.*, 2024, 15, 16917

All publication charges for this article have been paid for by the Royal Society of Chemistry

Helically chiral multiresonant thermally activated delayed fluorescent emitters and their use in hyperfluorescent organic light-emitting diodes†

Jingxiang Wang,^{‡a} Dongyang Chen,^{‡abc} Juan Manuel Moreno-Naranjo,^{‡d} Francesco Zinna,^{‡e} Lucas Frédéric,^f David B. Cordes,^{‡a} Aidan P. McKay,^{‡a} Matthew J. Fuchter,^{‡d} Xiaohong Zhang^{‡*bc} and Eli Zysman-Colman^{‡*a}

Chiral multiresonant thermally activated delayed fluorescence (MR-TADF) materials show great potential as emitters in circularly polarized (CP) organic light-emitting diodes (CP-OLEDs) owing to their bright and narrowband CP emission. Here, two new chiral MR-TADF emitters **tBuPh-BN** and **DPA-tBuPh-BN** possessing intrinsically helical chirality have been synthesized and studied. The large steric interactions between the *tert*-butylphenyl groups not only induce the helical chirality but also provide a notable configurational stability to the enantiomers. Racemic mixtures of **tBuPh-BN** and **DPA-tBuPh-BN** show narrowband emission at 490 and 477 nm with full-width at half maximum (FWHM) of 25 and 28 nm and photoluminescence quantum yields, Φ_{PL} , of 85 and 54% in toluene. The separated enantiomers of **tBuPh-BN** and **DPA-tBuPh-BN** show symmetric circularly polarized luminescence (CPL) with respective dissymmetry factors $|g_{\text{PL}}|$ values of 1.5×10^{-3} and 0.9×10^{-3} . The hyperfluorescence organic light-emitting diodes (HF-OLEDs) with **tBuPh-BN** and **DPA-tBuPh-BN** acting as terminal emitters and 2,3,4,5,6-penta-(9*H*-carbazol-9-yl)benzonitrile (5CzBN) as their assistant dopant exhibited, respectively, maximum external quantum efficiencies (EQE_{max}) of 20.9 and 15.9% at 492 and 480 nm with FWHM of 34 and 38 nm. This work demonstrates a strategy for developing intrinsically helically chiral MR-TADF emitters possessing significant configurational stability, which can be used in HF-OLEDs.

Received 28th May 2024
Accepted 14th September 2024

DOI: 10.1039/d4sc03478c

rsc.li/chemical-science

Introduction

Chiral molecules emitting circularly polarized luminescence (CPL) have been widely investigated for their promising applications in three-dimensional (3D) displays, optical data storage

and optical spintronics applications.^{1–4} In addition, this class of emitters has garnered significant interest as CPL offers a tantalizing solution to increasing the effective efficiency of organic light-emitting diodes (OLEDs)⁵ that contain anti-glare filters, which are required to improve the viewing contrast by limiting the reflection of external light.^{6–8} This requires materials to emit CPL selectively of one handedness. The propensity for CPL to possess a particular handedness is quantified by the dissymmetry factor g_{PL} , which is described by eqn (1):

$$g_{\text{PL}} = 2 \frac{(I_{\text{L}} - I_{\text{R}})}{(I_{\text{L}} + I_{\text{R}})} \quad (1)$$

where I_{L} and I_{R} refer to the intensities of left- and right-handed light, respectively. Pure left- or right-handed light is obtained when g_{PL} reaches +2 or −2. For a chiral emissive material to be relevant for practical applications such as OLEDs, the $|g_{\text{PL}}|$ should be as high as possible,⁹ the photoluminescence quantum yield (Φ_{PL}) should be high, and emission should be narrowband.

Organic thermally activated delayed fluorescence (TADF) materials have been widely explored as emitters in OLEDs over the past decade because of their ability to harvest both triplet and singlet excitons to produce light, leading to OLEDs with TADF emitters that can achieve 100% internal quantum

^aOrganic Semiconductor Centre, EaStCHEM School of Chemistry, University of St Andrews, St Andrews, Fife, KY16 9ST, UK. E-mail: eli.zysman-colman@st-andrews.ac.uk; Fax: +44 1334 463808; Tel: +44 1334 463826

^bInstitute of Functional Nano & Soft Materials (FUNSOM), Joint International Research Laboratory of Carbon-Based Functional Materials and Devices, Soochow University, Suzhou, Jiangsu, 215123, P. R. China

^cJiangsu Key Laboratory of Advanced Negative Carbon Technologies, Soochow University, Suzhou, Jiangsu, 215123, P. R. China

^dDepartment of Chemistry, Molecular Sciences Research Hub, Imperial College London, White City Campus, London, W12 0BZ, UK. E-mail: m.fuchter@imperial.ac.uk

^eDipartimento di Chimica e Chimica Industriale, Università di Pisa, 56124 Pisa, Italy

^fUniversité Paris-Saclay, ENS Paris-Saclay, CNRS, PPSM, 91190, Gif-sur-Yvette, France

† Electronic supplementary information (ESI) available: ¹H and ¹³C NMR spectra, HRMS, HPLC and EA of all target compounds; supplementary computational data, photophysical data and devices data; the structures and properties of all the chiral MR-TADF emitters. CCDC 2356677 and 2356678. For ESI and crystallographic data in CIF or other electronic format see DOI: <https://doi.org/10.1039/d4sc03478c>

‡ These authors contributed equally to this work.

efficiency (IQE).^{10,11} Multi-resonant TADF emitters, a sub-class of TADF materials, show characteristically narrowband emission and high Φ_{PL} due to their rigid structures and their possessing an emissive S_1 state of short-range charge transfer (SRCT) character.¹² Since the first reported example of a MR-TADF emitter by Hatakeyama and co-workers in 2016,¹³ now more than 250 examples of MR-TADF emitters for OLEDs have been reported, with many examples of devices showing maximum external quantum efficiencies (EQE_{max}) of >30%.^{14,15} Of the reported MR-TADF emitters there are a small number that are chiral and CPL-active.

There are mainly two strategies for designing chiral MR-TADF emitters.¹⁶ The first one is chiral perturbation, which refers to introducing a peripheral chiral unit into an achiral MR-TADF structure that does not directly participate in the radiative S_1 - S_0 transition. Li *et al.* reported the first two chiral MR-TADF emitters **OBN-2CN-BN** and **OBN-4CN-BN** containing (*R*)/(*S*)-octahydro-binaphthol ((*R*)/(*S*)-OBN) units (Fig. S40, Table S6†).¹⁷ These two compounds emit at λ_{PL} of 498 and 510 nm (full-width at half maximum, FWHM of 32 and 35 nm), have Φ_{PL} of 95 and 90% and $|g_{\text{PL}}|$ values of 9.1×10^{-4} and 1.04×10^{-3} in 3 wt% doped films in PhCzBCz, respectively. Although materials based on chiral perturbation are generally easy to synthesize and do not need enantiomer separation as the chiral unit that is incorporated is generally already enantiopure, they tend to show weak CPL signals.^{16,18} The second strategy involves the design of MR-TADF emitters that possess an intrinsically chiral skeleton.^{19,20} To date, there are only a few examples of chiral MR-TADF emitters based on this strategy. They have either point,^{21–24} axial,^{25–28} planar,^{29,30} or helically^{31–43} chiral skeletons (Fig. S40, Table S6†). Of particular note, Guo *et al.* developed a large helicene-based chiral MR-TADF emitter **BN[9]H**, which emits at λ_{PL} of 578 nm (FWHM of 47 nm) and has a Φ_{PL} of 98% in toluene.⁴² The $|g_{\text{PL}}|$ is 5.8×10^{-3} in toluene, which is the highest value among all the reported chiral MR-TADF emitters to date. The CP-OLEDs with **P-BN[9]H** emitted at λ_{EL} of 580 nm and showed an EQE_{max} of 35.4% and a low efficiency roll-off (EQE₁₀₀ of 33.1%). The g_{EL} value of 6.2×10^{-3} was of similar magnitude to the $|g_{\text{PL}}|$.

Here, we report two new chiral MR-TADF emitters **tBuPh-BN** and **DPA-tBuPh-BN** (Fig. 1) based on the CzBN core of **DtBuCzB**,⁴⁴ a compound that shows narrowband emission at 481 nm (FWHM of 22 nm) and high Φ_{PL} of 91% in toluene. The *tert*-butylphenyl groups are introduced to induce helical chirality and the large steric hindrance between them is hypothesized to inhibit the racemization between the two helically chiral enantiomers. A diphenylamine (DPA) group is introduced to the *para* position of the boron-substituted phenyl ring in **DPA-tBuPh-BN** to explore the effect that peripheral units have on the optoelectronic properties of these chiral MR-TADF compounds. **tBuPh-BN** and **DPA-tBuPh-BN** exhibit narrow sky-blue emission at 490 nm (FWHM of 25 nm) and 477 nm (FWHM of 28 nm) and have Φ_{PL} of 85 and 54% in toluene, respectively. Due to their large ΔE_{ST} values of 0.36 and 0.43 eV for **tBuPh-BN** and **DPA-tBuPh-BN**, they show long delayed lifetimes, τ_{d} , of 41 and 60 ms in 2 wt% doped films in SF3-TRZ, respectively. The resolved enantiomers of **tBuPh-BN** and **DPA-**

tBuPh-BN show symmetric CPL, with $|g_{\text{PL}}|$ values of 1.5×10^{-3} and 0.9×10^{-3} , respectively. Hyperfluorescence (HF) OLEDs using 2,3,4,5,6-penta-(9*H*-carbazol-9-yl)benzonitrile (**5CzBN**) as the TADF assistant dopant and with **tBuPh-BN** and **DPA-tBuPh-BN** as the terminal emitters showed narrowband emission at λ_{EL} of 492 and 480 nm (FWHM of 34 and 38 nm) and EQE_{max} of 20.9 and 15.9%, respectively.

Results & discussion

Synthesis

The synthesis of **tBuPh-BN** and **DPA-tBuPh-BN** is outlined in Fig. S1†. The intermediate **1** was prepared under Suzuki–Miyaura cross-coupling conditions in 64% yield, which was then reacted through a nucleophilic aromatic substitution to afford **2** and **3** in 74 and 97% yield, respectively, while compound **4** was prepared by a palladium-catalyzed Buchwald–Hartwig amination between compound **3** and di-*p*-tolylamine in 60% yield. **tBuPh-BN** and **DPA-tBuPh-BN** were obtained from **2** and **4**, respectively, following an electrophilic borylation in 17 and 11% yield, respectively. The relatively low yields can be mainly attributed to the large steric hindrance around the boron atom. Their identity and purity were characterized using melting point determination, ¹H and ¹³C nuclear magnetic resonance (NMR) spectroscopy, high-resolution mass spectrometry (HRMS), high-performance liquid chromatography (HPLC), and elemental analysis (EA) (Fig. S2–S23†). The structures of racemic **tBuPh-BN** and **DPA-tBuPh-BN** were confirmed by single crystal X-ray diffraction analysis (Fig. 2, Table S1†). X-ray quality crystals were obtained from slow evaporation of THF:MeOH solutions of **tBuPh-BN** and **DPA-tBuPh-BN**. The structure of **DPA-tBuPh-BN** was found to be enantiopure and showing just the *M*-enantiomer, despite the crystals having been grown from the racemic mixture from synthesis. Both emitters have conformations distorted away from planarity due to the large steric hindrance between the two proximal *tert*-butylphenyl groups. This forces a twist onto the core of the molecule, carbazole groups being inclined at 40.25(5) and 37.92(3)° for **tBuPh-BN** and **DPA-tBuPh-BN**, respectively, endowing them with helical chirality. Both structures showed only weak interactions between adjacent molecules. Molecules of **tBuPh-BN** interacted *via* a combination of mutually supporting π - π and edge-to-face $\text{CH}\cdots\pi$ interactions, with centroid \cdots centroid distances of 3.787(2) Å, and $\text{H}\cdots$ centroid distance of 2.68 Å (corresponding C \cdots centroid separation of 3.572(4) Å). These interactions form discrete dimers of **tBuPh-BN**. In contrast, molecules of **DPA-tBuPh-BN** display two sets of $\text{CH}_{\text{methyl}}\cdots\pi$ interactions between, with $\text{H}\cdots$ centroid distances of 2.70 and 2.78 Å (corresponding C \cdots centroid separations of 3.642(3) and 3.411(3) Å). These interactions in combination led to the formation of weakly interacting two-dimensional sheet structures. The enantiomers of **tBuPh-BN** and **DPA-tBuPh-BN** were separated by chiral HPLC, to afford ee. 99% for (*P*)-**tBuPh-BN**, 97% for (*M*)-**tBuPh-BN**, 99% for (*P*)-**DPA-tBuPh-BN** and 99% for (*M*)-**DPA-tBuPh-BN** (Fig. S24 and S25†). The absolute configurations (*P* and *M*) here were tentatively determined by comparing the measured and simulated circular dichroism



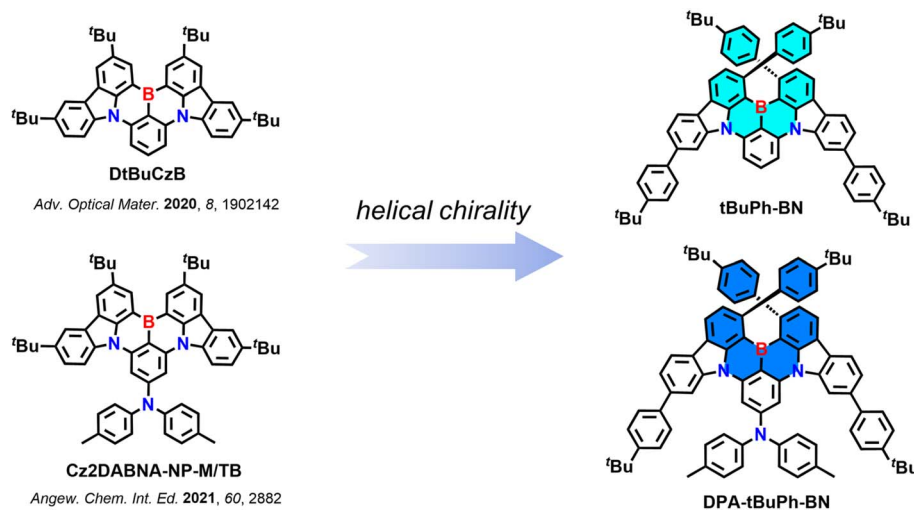


Fig. 1 Molecular design of tBuPh-BN and DPA-tBuPh-BN.

(CD) spectra in toluene solution (Fig. S26[†]). **tBuPh-BN** and **DPA-tBuPh-BN** are thermally stable and have high thermal decomposition temperatures (T_d , corresponding to 5% weight loss) of 488 and 493 °C, respectively. No glass transition temperature was observed in the differential scanning calorimetry (DSC) measurement of either compound (Fig. S27[†]).

Theoretical calculations

The optimized ground-state geometries of **tBuPh-BN** and **DPA-tBuPh-BN** were calculated using Density Functional Theory (DFT) at the PBE0/6-31G(d,p) level (Fig. S28[†]).^{45,46} The highest occupied molecular orbital (HOMO) and lowest unoccupied molecular orbital (LUMO) of **tBuPh-BN** are both located on the CzBN core. The calculated HOMO and LUMO energies of **tBuPh-**

BN are $-5.43/-1.78$ eV and the energy gap (ΔE) is 3.65 eV. The slightly deeper HOMO and LUMO levels compared to those of **DtBuCzB** (HOMO = -5.28 eV, LUMO = -1.64 eV)⁴⁴ may originate from an inductively electron-withdrawing effect from the *tert*-butylphenyl groups. By contrast, the HOMO of **DPA-tBuPh-BN** is localized on the electron-donating DPA moiety, and this leads to a destabilization of the both the HOMO and LUMO levels at -5.23 and -1.66 eV, respectively.

The excited-state energies and difference densities were calculated using Spin-Component Scaling second-order algebraic diagrammatic construction (SCS-(ADC)2/cc-pVDZ).^{47,48} As shown in Fig. 3, both emitters have difference density patterns for both the S_1 and T_1 states that are reminiscent of SRCT states localized on the CzBN core. **tBuPh-BN** and **DPA-tBuPh-BN** have

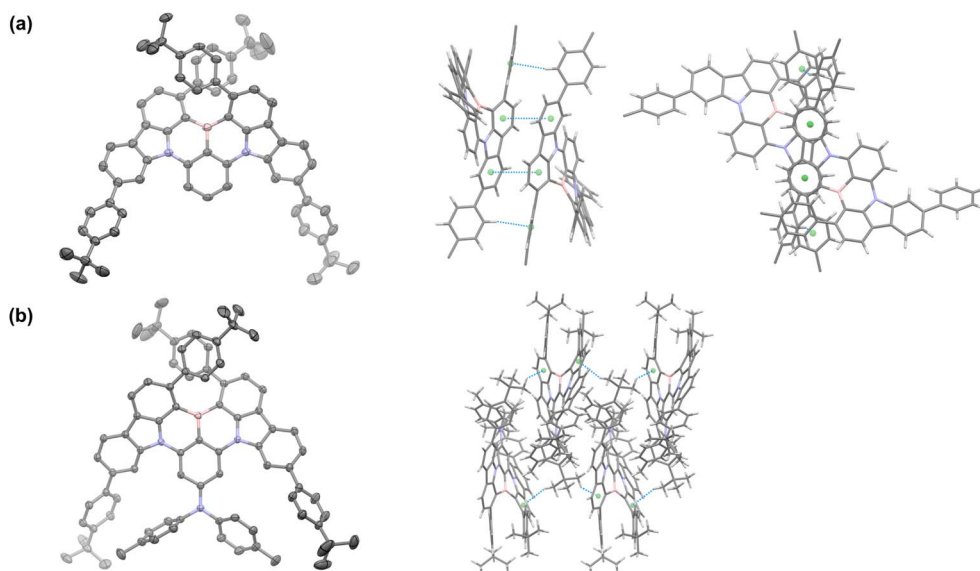


Fig. 2 Thermal ellipsoid plot of the structures and intermolecular interactions of (a) **tBuPh-BN** and (b) **DPA-tBuPh-BN**. Ellipsoids are displayed at the 50% probability level, solvent molecules, minor components of disorder and hydrogens are omitted for clarity.





Fig. 3 Difference density plots and energies of S_1 and T_1 calculated in the gas phase at SCS-(ADC)2/cc-pVDZ level, respectively, for (a) **tBuPh-BN** and (b) **DPA-tBuPh-BN** (Blue indicates an area of decreased electron density while yellow indicates increased electronic density between the ground and excited states).

S_1/T_1 energies of 3.01/2.89 eV and 3.03/2.92 eV, respectively, and the corresponding ΔE_{ST} values are similar at 0.12 and 0.11 eV, respectively. Spin-orbit coupling matrix elements (SOCME) were also calculated based on the optimized T_1 geometries at the PBE0/6-31G(d,p) level (Fig. S28†). **tBuPh-BN** and **DPA-tBuPh-BN** have similar SOCME values of 0.17, 0.35, 0.23 and 0.20, 0.33, 0.19 cm^{-1} for the S_1-T_1 , S_1-T_2 , S_1-T_3 transitions, respectively. The larger SOCME and smaller energy gaps between S_1 and T_2 for both **tBuPh-BN** and **DPA-tBuPh-BN** indicate that RISC may proceed via T_2 to S_1 .^{49–52}

Optoelectronic properties

The HOMO and LUMO values of **tBuPh-BN** and **DPA-tBuPh-BN** were extrapolated from the electrochemistry measurements in degassed dichloromethane with 0.1 M [$^n\text{Bu}_4\text{N}$]PF₆ as the supporting electrolyte and Fe/Fe⁺ as the internal reference (0.46 V vs. SCE)⁵³ (Fig. S29†). The electrochemical data are summarized in Table S2.† The cyclic voltammograms of both **tBuPh-BN** and **DPA-tBuPh-BN** show reversible oxidation waves. **tBuPh-BN** has an oxidation potential, E_{ox} , of 1.19 V vs. SCE, obtained from the peak of the differential pulse voltammogram. The corresponding HOMO energy is -5.53 eV, which is close to the HOMO of **DtBuCzB** (**DtCzB**) (-5.40 eV),^{44,54} indicating that it is localized on the CzBN core. By contrast, the E_{ox} of **DPA-tBuPh-BN** is cathodically shifted to 0.97 V vs. SCE (HOMO of -5.31 eV). This value is very similar to the HOMO of **tDPA-DtCzB**, which contains a 4,4'-di-*tert*-butylphenylamine donor (HOMO of -5.24 eV), indicating that oxidation occurs at the amine group.⁵⁴ Both **tBuPh-BN** and **DPA-tBuPh-BN** show reversible reduction waves with reduction potentials (E_{red}) of -1.77 and -1.85 V, respectively; the corresponding LUMO energies are -2.57 and -2.49 eV. The small differences in LUMO levels compared to those of **DtCzB** (-2.61 eV) and **tDPA-DtCzB** (-2.38 eV)⁵⁴ indicate that the LUMO in both **tBuPh-BN** and **DPA-tBuPh-BN** is situated

on the DtCzB core and that the amine donor group in **DPA-tBuPh-BN** promotes a destabilization of the LUMO level compared to **tBuPh-BN**. The corresponding ΔE values are calculated to be 2.96 and 2.82 eV, respectively. The trends in orbital energies align well with the DFT calculations ($-5.43/-1.78$ eV and $-5.23/-1.66$ eV, respectively).

The ultraviolet-visible (UV-vis) absorption and photoluminescence (PL) properties of the two emitters were first investigated in toluene at room temperature (Fig. 4a). The absorption spectra of **tBuPh-BN** and **DPA-tBuPh-BN** show low-energy bands at 463 and 455 nm, respectively, which are attributed to the SRCT S_0-S_1 transitions and are close to that of **DtBuCzB** (λ_{abs} of 467 nm).⁴⁴ The higher molar absorptivity (ϵ) of this SRCT band in **tBuPh-BN** ($5.2 \times 10^4 \text{ M}^{-1} \text{ cm}^{-1}$) than that in **DPA-tBuPh-BN** ($4.2 \times 10^4 \text{ M}^{-1} \text{ cm}^{-1}$) is correlated to the higher calculated oscillator strength of the S_0-S_1 transitions (0.28 for **tBuPh-BN** and 0.25 for **DPA-tBuPh-BN**). **tBuPh-BN** is a narrow-band emitter, with its photoluminescence peaking at λ_{PL} of 490 nm and having a FWHM, of 25 nm (0.13 eV). The emission properties are comparable to those of **DtBuCzB** (λ_{PL} of 481 nm, FWHM of 22 nm in toluene),⁴⁴ which illustrates that the nature of the S_1 state is the same in these compounds. By contrast for **DPA-tBuPh-BN**, the DPA donor positioned *para* to the boron atom reduces its electron-withdrawing character and weakens the SRCT transition localized on the CzBN core,⁵⁵ resulting in a blue-shifted emission band at 477 nm, which also aligns with the slightly higher calculated S_1 energy (3.03 eV) compared to that of **tBuPh-BN** (3.01 eV) (Fig. 3). The slightly broader FWHM of 28 nm/0.15 eV can be attributed to the larger degree of geometry relaxation on the DPA group between ground and excited states. The photophysics of **DPA-tBuPh-BN** is reminiscent of that of **tDPA-DtCzB** (λ_{PL} of 470 nm and FWHM of 21 nm in toluene).⁵⁴ The larger Stokes shifts of **tBuPh-BN** (27 nm) and **DPA-tBuPh-BN** (22 nm) compared to that of **DtBuCzB** (14 nm)⁴⁴



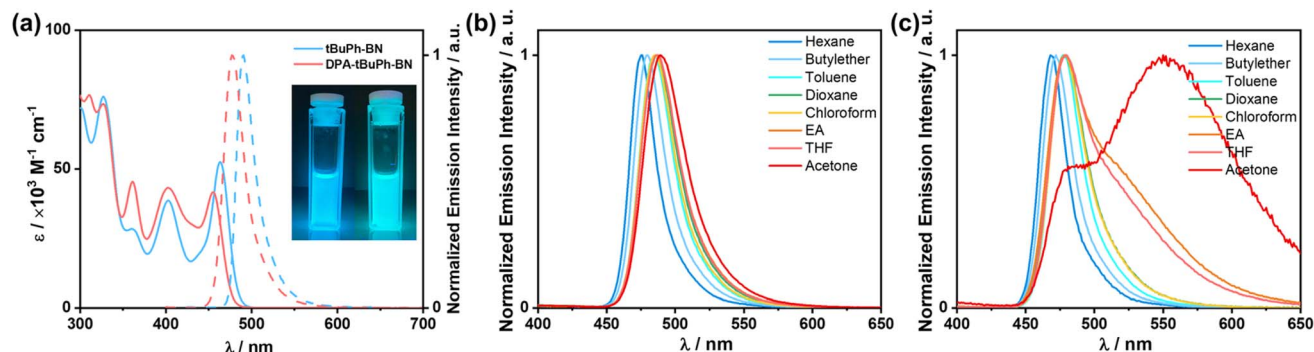


Fig. 4 (a) UV-vis absorption spectra and PL spectra of *t*BuPh-BN and DPA-*t*BuPh-BN in toluene at 300 K; inset: photos of *t*BuPh-BN (right) and DPA-*t*BuPh-BN (left) in toluene excited at 365 nm. PL spectra of (b) *t*BuPh-BN and (c) DPA-*t*BuPh-BN in different solvents at 300 K. ($\lambda_{\text{exc}} = 340$ nm).

and *t*DPA-DtCzB (14 nm)⁵⁴ indicate a larger degree of structural relaxation between ground and excited states due to the introduction of the *tert*-butylphenyl groups. *t*BuPh-BN and DPA-*t*BuPh-BN have contrasting Φ_{PL} values in degassed toluene of 85 and 54%, respectively. A solvatochromic study on the impact of solvent polarity on the PL spectra of *t*BuPh-BN and DPA-*t*BuPh-BN is shown in Fig. 4b and c. *t*BuPh-BN shows a very small degree of positive solvatochromism, which confirms that the SRCT character of the S_1 state is conserved across all these solvents. By contrast, there are two regimes of behavior for DPA-*t*BuPh-BN, where in low polarity solvents emission from the SRCT state dominates but in higher polarity solvents dual emission is observed. This is due to emission originating from both the SRCT state and a long-range charge-transfer state (LRCT) from the strong DPA donor to the weak CzBN acceptor as this latter state becomes increasingly stabilized in higher polarity solvents, a behavior that was observed previously in donor-substituted DiKTA derivatives.⁵⁶ The unchanging PL spectra of DPA-*t*BuPh-BN in acetone under different concentrations confirm that the latter emission band is not from aggregates (Fig. S30†).

The steady-state PL (SS PL) and phosphorescence (Ph) spectra were measured in 2-MeTHF at 77 K to determine the singlet and triplet energies and, thus, the ΔE_{ST} values of *t*BuPh-BN and DPA-*t*BuPh-BN (Fig. S31†). The singlet and triplet energies were determined from the onsets of the SS PL and Ph spectra, respectively. The S_1/T_1 energies for *t*BuPh-BN and DPA-*t*BuPh-BN are 2.60/2.24 and 2.71/2.28 eV, respectively, resulting in ΔE_{ST} values of 0.36 and 0.43 eV. Although their S_1 energies are similar to those of DtBuCzB (2.66 eV) and *t*DPA-DtCzB (2.72 eV), their T_1 energies are much lower (DtBuCzB (2.53 eV) and *t*DPA-DtCzB (2.61 eV)), which leads to much larger ΔE_{ST} values than the 0.13 eV for DtBuCzB and 0.11 eV for *t*DPA-DtCzB.^{44,54} To explore the origin for the divergent T_1 energies and ΔE_{ST} values compared to the literature reference compounds, the S_1 and T_1 energies of the fragments, 2,7-diphenyl-9H-carbazole (2,7-PhCz) and 3,6-diphenyl-9H-carbazole (3,6-PhCz), were calculated using time-dependent DFT within the Tamm-Dancoff approximation (Fig. S32†). Both 2,7-PhCz and 3,6-PhCz have almost the same S_1 energies of around 4 eV; however, as the electron

density of T_1 in 2,7-PhCz is delocalized across the whole molecule, this leads to a much-stabilized T_1 energy of 3.04 eV compared to that of 3,6-PhCz (3.33 eV). Thus, this explains the much larger ΔE_{ST} values for *t*BuPh-BN and DPA-*t*BuPh-BN as there is a much more stabilized locally-excited state situated on the 2,7-PhCz donor groups. The time-resolved PL decays in degassed toluene are shown in Fig. S31c.† The emission of both *t*BuPh-BN and DPA-*t*BuPh-BN decay with monoexponential kinetics with short lifetimes (τ_{PL}) of 5.8 and 4.4 ns, respectively. Due to the large ΔE_{ST} values and the competing non-radiative decay processes with ISC/RISC,⁵⁷ no delayed emission was observed in toluene solution.

The photophysical properties of thin films were then investigated. The host 2-(9,9'-spiro[fluoren]-3-yl)-4,6-diphenyl-1,3,5-triazine (SF3-TRZ) was chosen because of its suitably high triplet energy ($E_{\text{T}} = 2.80$ eV) and ability to balance charge transport in a HF OLED using 5CzBN as the assistant dopant.⁵⁸ The absolute Φ_{PL} values at different doping concentrations were measured under a nitrogen atmosphere (Table S3†). Both compounds show a propensity to aggregate that is reflected in their lower Φ_{PL} (67% to 42% for *t*BuPh-BN and 47% to 30% for DPA-*t*BuPh-BN) and slightly broader and red-shifted emission (490 to 496 nm for *t*BuPh-BN and 484 to 491 nm for DPA-*t*BuPh-BN) of the 1, 2, 4 and 10 wt% doped films compared to the results from toluene solution (Φ_{PL} of 85% and 54%, λ_{PL} of 490 and 477 nm, respectively) (Fig. S33†). The 2 wt% doped films of *t*BuPh-BN and DPA-*t*BuPh-BN in SF3-TRZ emit at λ_{PL} of 496 and 487 nm (FWHMs of 31 nm/0.16 eV and 31 nm/0.16 eV), respectively (Fig. 5a). At 300 K under vacuum, the time-resolved PL decays of *t*BuPh-BN and DPA-*t*BuPh-BN show biexponential kinetics, with a dominant prompt lifetime, τ_{p} , of 5.9 and 4.6 ns and long τ_{d} of 41 and 60 ms, respectively (Table 1). The largely decreased delayed components to the lifetime of *t*BuPh-BN with an increase in the doping concentration from 0.5 to 2 wt% doped film and the neat film indicate that the delayed emission originates from the isolated molecule rather than from aggregates (Fig. S34†). An analysis of the temperature-dependent time-resolved PL decays under vacuum reveal an increasing intensity of the delayed emission with increasing temperature that is characteristic of TADF (Fig. 5b and c).





Fig. 5 (a) Steady-state PL spectra at 300 K of 2 wt% doped film of emitters in SF3-TRZ ($\lambda_{\text{exc}} = 340$ nm). Temperature-dependent time-resolved PL decays of in 2 wt% doped film of (b) **tBuPh-BN** and (c) **DPA-tBuPh-BN** in SF3-TRZ (inset figures are PL decays of the prompt components at 300 K) ($\lambda_{\text{exc}} = 375$ nm).

The chiroptical properties of (*P*)/(*M*)-**tBuPh-BN** and (*P*)/(*M*)-**DPA-tBuPh-BN** were investigated in solution. As shown in Fig. 6a and d, both emitters display typical mirror image CD spectra between *P* and *M* enantiomers. The maximum absorption dissymmetry factor g_{abs} values are $+5.5 \times 10^{-3}$ and -5.4×10^{-3} at 385 nm for (*P*)/(*M*)-**tBuPh-BN** and $+5.5 \times 10^{-3}$ and -5.1×10^{-3} at 382 nm for (*P*)/(*M*)-**DPA-tBuPh-BN**, respectively. Both emitters also show mirror symmetric CPL spectra in THF solutions (Fig. 6c and f) with g_{PL} values of $+1.5 \times 10^{-3}$ and -1.3×10^{-3} for (*P*)/(*M*)-**tBuPh-BN** and $+0.9 \times 10^{-3}$ and -0.8×10^{-3} for (*P*)/(*M*)-**DPA-tBuPh-BN**, respectively. To better understand the origin of the differing g_{PL} values between **tBuPh-BN** and **DPA-tBuPh-BN**, TDA-DFT calculations starting from the

optimized S_1 geometries were performed to predict the g_{PL} values in THF (Table S4†). The M062X/6-31G(d,p) level of theory was chosen here because it accurately predicts the SRCT character of the S_1 state of **DPA-tBuPh-BN**, while PBE0/6-31G(d,p) calculations incorrectly predict that this state should have LRCT character (Fig. S35†). The calculated g_{PL} values of (*M*)-**tBuPh-BN** and (*M*)-**DPA-tBuPh-BN** are -1.6×10^{-3} and -0.67×10^{-3} , respectively, which align well with the experimental values. Both emitters have similar predicted electric transition dipole moment $|\mu|$ and angles between μ and the magnetic transition dipole moment m . The lower g_{PL} value of (*M*)-**DPA-tBuPh-BN** therefore mainly originates from the lower magnitude of $|m|$. CPL brightness (B_{CPL}) was also estimated as $B_{\text{CPL}} = \varepsilon \times \Phi_{\text{PL}} \times g_{\text{PL}}/2$.⁵⁹ The ε and Φ_{PL}



Fig. 6 (a) CD spectra and (b) g_{abs} values of **tBuPh-BN** recorded in 5×10^{-6} mol L⁻¹ toluene solution. (c) g_{PL} values of **tBuPh-BN** recorded in 10^{-5} mol L⁻¹ THF solution. (d) CD spectra and (e) g_{abs} values of **DPA-tBuPh-BN** recorded in 5×10^{-6} mol L⁻¹ toluene solution. (f) g_{PL} values of **DPA-tBuPh-BN** recorded in 10^{-5} mol L⁻¹ THF solution.



values of **tBuPh-BN** and **DPA-tBuPh-BN** in THF are $3.9 \times 10^4 \text{ M}^{-1} \text{ cm}^{-1}$, 66%, and $3.8 \times 10^4 \text{ M}^{-1} \text{ cm}^{-1}$, 49%, respectively. The calculated B_{CPL} values of (*P*)-**tBuPh-BN** and (*P*)-**DPA-tBuPh-BN** are 19.3 and $8.4 \text{ M}^{-1} \text{ cm}^{-1}$, respectively. These values are at the high end of those calculated for helicenes⁵⁹ and comparable to the reported high-performance chiral MR-TADF emitters,^{35,40,41,43} illustrating that **tBuPh-BN** and **DPA-tBuPh-BN** are efficient CPL-active TADF helicenes. To explore the stereochemical stability of **tBuPh-BN** and **DPA-tBuPh-BN**, the racemization energy barrier of the helicene moiety was calculated using DFT at the M062X/6-31G(d,p) level of theory (Fig. S36†). The calculated high energy barrier of $\Delta G^\ddagger = 48.28 \text{ kcal mol}^{-1}$ enables the chiral separation of **tBuPh-BN** and **DPA-tBuPh-BN**.^{33,35,41,42} In addition, no racemization was observed at 90 °C in toluene over more than 5 hours as the CD signals of (*P*)-**tBuPh-BN** and (*P*)-**DPA-tBuPh-BN** remained constant (Fig. S37†).³⁸ Both computational and experimental results indicate that the large steric hindrance between the top two *tert*-butylphenyl groups provide a notable stereochemical stability to the enantiomers.

Organic light-emitting diodes

We next fabricated vacuum-deposited OLEDs with **tBuPh-BN** and **DPA-tBuPh-BN** using a device structure of indium tin oxide (ITO)/1,4,5,8,9,11-hexaazatriphenylenehexacarbonitrile (HATCN, 5 nm)/1,1-bis[(di-4-tolylamino)phenyl]cyclohexane (TAPC, 30 nm)/tris(4-carbazoyl-9-ylphenyl)amine (TCTA, 10 nm)/mCP (5 nm)/emitting layer (EML) (20 nm)/1,3,5-tris(3-pyridyl-3-phenyl)benzene (TmPyPB, 40 nm)/lithium fluoride (LiF, 1 nm)/aluminum (Al, 100 nm). Here, HATCN was used as the hole injection layer, TAPC and TCTA as the hole transporting layers, mCP as an exciton blocking layer, TmPyPB as an electron transporting layer, and LiF was used to reduce the work function of the top Al electrode. The OLED device stack and the chemical structures of the organic layers are shown in Fig. 7a and b. The device data are summarized in Table 2.

We first fabricated OLEDs with a higher concentration of 4 wt% emitters in SF3-TRZ as the EML as it was hypothesized that a higher concentration of emitter would contribute to improve the charge balance and enlarge the exciton recombination zone. Electroluminescence (EL) spectra, current density–voltage–luminance (*JVL*) curves and EQE vs. luminance curves are shown in Fig. 7c–e. **tBuPh-BN** and **DPA-tBuPh-BN** emitted narrowband green and sky-blue light at λ_{EL} of 496 and 484 nm, each having FWHM of 34 nm; the EL spectra are close to the corresponding PL spectra (Fig. 5). Due in part to their long delayed lifetimes the devices with **tBuPh-BN** and **DPA-tBuPh-BN**

showed low EQE_{max} of 4.9 and 4.8% and severe efficiency roll-off (EQE₁₀₀ of both 2.8% and EQE₁₀₀₀ of 1.7 and 1.8%, respectively). The Commission International de l'Éclairage, CIE, coordinates for the devices with **tBuPh-BN** and **DPA-tBuPh-BN** were (0.10, 0.50) and (0.11, 0.31). The OLEDs with 2 wt% emitters were also fabricated for comparison. Due to an incomplete energy transfer from the host to the emitter, the device with **DPA-tBuPh-BN** exhibited another blue emission band at around 420 nm, originating from emission from SF3-TRZ (Fig. S37†). When compared to the OLEDs with 4 wt% emitters, although the devices with 2 wt% of **tBuPh-BN** and **DPA-tBuPh-BN** showed bluer emission at λ_{PL} of 492 and 480 nm [CIE coordinates of (0.10, 0.45) and (0.12, 0.22)] due to the lower contribution to the emission from aggregates, their maximum luminance (L_{max}) (2217 and 990 cd m^{-2}) and EQE_{max} (4.6% for both devices) were decreased. This may arise from a limited exciton recombination zone in the EML of these devices. The performance and data are summarized in Table S5.†

In a bid to improve the device performance and given the narrowband emission and high Φ_{PL} values for **tBuPh-BN** and **DPA-tBuPh-BN**, HF OLEDs were then fabricated (Fig. 7a). **5CzBN** was used as the TADF assistant dopant because of its high Φ_{PL} of 70%, fast k_{RISC} of $1.13 \times 10^5 \text{ s}^{-1}$, and a strong overlap between the absorption spectra of **tBuPh-BN** and **DPA-tBuPh-BN** and the PL spectrum of **5CzBN** in toluene (Fig. S39a†).⁶⁰ An optimized doping ratio of 2 wt% emitters: 12 wt% **5CzBN**: 86 wt% SF3-TRZ was identified to be used as the EML as this formulation minimized the chance for triplet excitons from the host to transfer to the emitters and permitted an efficient Förster resonance energy transfer from **5CzBN** to the emitters (Fig. S39b and c†) while conserving their narrowband emission. As shown in Fig. 7, the HF devices with **tBuPh-BN** and **DPA-tBuPh-BN** showed narrowband emission at λ_{PL} of 492 and 480 nm and FWHMs of 34 nm (0.17 eV) and 38 nm (0.20 eV). The corresponding CIE coordinates were (0.11, 0.41) and (0.13, 0.29), respectively, which are similar to those of the 2 wt% emitter OLEDs (Fig. S38, Table S5†). The turn-on voltages (V_{on}) were reduced from 3.5 and 3.7 V to 3.1 and 3.3 V and the EQE_{max} values were significantly improved to 20.9 and 15.9% for the HF devices with **tBuPh-BN** and **DPA-tBuPh-BN**, respectively. The relatively higher EQE_{max} for the HF OLED with **tBuPh-BN** can be attributed to the higher Φ_{PL} of the emitter and the larger overlap between the absorption spectra of the MR-TADF emitters and the PL spectrum of **5CzBN** (Spectral overlap integrals^{61,62} were estimated to be $6.0 \times 10^{13} \text{ M}^{-1} \text{ cm}^{-1} \text{ nm}^4$ for **tBuPh-BN** and $4.2 \times 10^{13} \text{ M}^{-1} \text{ cm}^{-1} \text{ nm}^4$ for **DPA-tBuPh-BN**). Despite their higher EQE_{max}, the efficiency roll-off of the HF devices remained severe

Table 1 Photophysical data of **tBuPh-BN** and **DPA-tBuPh-BN**

Compound	$\lambda_{\text{abs}}^a/\text{nm}$	λ_{PL}^b (FWHM)/nm	$\Delta E_{\text{ST}}^c/\text{eV}$	$ g_{\text{PL}} ^d$	$\Phi_{\text{PL}}^e/\%$	λ_{PL}^f (FWHM)/nm	τ_p^g/ns	τ_d^g/ms
tBuPh-BN	463	490 (25)	0.36	1.5×10^{-3}	85	496 (31)	5.9	41
DPA-tBuPh-BN	455	477 (28)	0.43	0.9×10^{-3}	54	487 (31)	4.6	60

^a In toluene. ^b In toluene at room temperature, $\lambda_{\text{exc}} = 340 \text{ nm}$. ^c In 2-MeTHF at 77 K, $\lambda_{\text{exc}} = 340 \text{ nm}$, $\Delta E_{\text{ST}} = E(S_1) - E(T_1)$. ^d In THF at room temperature, $\lambda_{\text{exc}} = 365 \text{ nm}$. ^e In degassed toluene at room temperature, $\lambda_{\text{exc}} = 350 \text{ nm}$. ^f In 2 wt% doped films in SF3-TRZ at 300 K under vacuum, $\lambda_{\text{exc}} = 340 \text{ nm}$. ^g In 2 wt% doped films in SF3-TRZ at 300 K under vacuum, $\lambda_{\text{exc}} = 375 \text{ nm}$.





Fig. 7 (a) Schematic of the device stack of the OLEDs; (b) chemical structures of the organic layers; (c) EL spectra recorded at 5 V, the insets are the photograph images of the HF devices for *t*BuPh-BN (left) and DPA-*t*BuPh-BN (right); (d) JVL characteristics; (e) EQE vs. luminance for the OLEDs.

Table 2 Device data of *t*BuPh-BN and DPA-*t*BuPh-BN

Traditional device ^a	V_{on}/V	λ_{EL}^c (FWHM)/nm	$L_{max}/cd\ m^{-2}$	$EQE_{max/100/1000}/\%$	$CIE^c(x, y)$
<i>t</i>BuPh-BN	3.5	496 (34)	2560	4.9/2.8/1.7	0.10, 0.50
DPA-<i>t</i>BuPh-BN	3.7	484 (34)	1650	4.8/2.8/1.8	0.11, 0.31
HF device^b					
<i>t</i>BuPh-BN	3.1	492 (34)	5850	20.9/9.8/7.1	0.11, 0.41
DPA-<i>t</i>BuPh-BN	3.3	480 (38)	3370	15.9/10.1/7.8	0.13, 0.29

^a 4 wt% emitters in SF3-TRZ as EMLs. ^b 2 wt% emitters and 12 wt% 5CzBN in SF3-TRZ as EMLs. ^c Recorded at 5 V.

(EQE_{100} of 9.8 and 10.1% and EQE_{1000} of 7.1 and 7.8% for the HF devices with *t*BuPh-BN and DPA-*t*BuPh-BN, respectively). Two possible explanations are that the competing processes of direct exciton recombination on the emitters or the short-range Dexter energy transfer from 5CzBN to that of the emitters are still strong.⁵⁴ The accumulation of triplet excitons would increase the probability of bimolecular excitonic quenching processes that manifest in severe efficiency roll-off in the devices.

Conclusions

Two new MR-TADF emitters *t*BuPh-BN and DPA-*t*BuPh-BN possessing intrinsically helical chirality have been designed and synthesized. The SCS-(ADC)2 calculations and the narrowband emission at 490 and 477 nm (FWHM of 25 and 28 nm) for *t*BuPh-BN and DPA-*t*BuPh-BN, respectively, in toluene corroborate an emission from a SRCT excited state. The large steric hindrance between two of the *tert*-butylphenyl groups provides

both molecules with significant thermal stability towards racemization, resulting in configurational stability even at 90 °C. As a result, the separated enantiomers of *t*BuPh-BN and DPA-*t*BuPh-BN show symmetric CD and CPL spectra, with PL dissymmetry factor values, $|g_{PL}|$, of 1.5×10^{-3} and 0.9×10^{-3} , respectively. Finally, the optimized HF-OLEDs with *t*BuPh-BN and DPA-*t*BuPh-BN as the terminal emitter achieved narrow-band sky-blue emission with EQE_{max} of 20.9 and 15.9%, respectively. This study illustrates the effect of the addition of sterically bulky groups at the 2 and 7 positions of carbazole on the properties of derived MR-TADF emitters on both the photophysical and chiroptical performance.

Data availability

The research data supporting this publication can be accessed at <https://doi.org/10.17630/3dbc2b86-2c76-464e-8423-cd5c95247a07>.



Author contributions

Jingxiang Wang performed the synthesis, the theoretical calculations, the optoelectronic characterization and wrote the original manuscript. The molecules were designed by Dr Lucas Frédéric. The crystal structures were solved by Dr Aidan P. McKay and Dr David B. Cordes. The OLEDs were fabricated by Dr Dongyang Chen. The chiroptical properties were measured by Juan Manuel Moreno-Naranjo and Dr Francesco Zinna. Prof. Matthew J. Fuchter, Prof. Xiaohong Zhang and Prof. Eli Zysman-Colman were responsible for supervision and financing the project and revised the manuscript. Prof. Eli Zysman-Colman managed the project.

Conflicts of interest

The authors declare no conflict of interest.

Acknowledgements

J. W. thanks the China Scholarship Council (202006250026). D. Chen thanks the support from China Postdoctoral Science Foundation (Grant No. 2022TQ0227) and Natural Science Foundation of Jiangsu Province, China (Grant No. BK20230508). We acknowledge support from the European Commission Research Executive Agency (Grant Agreement Number: 859752 HEL4CHIR-OLED H2020-MSCA-ITN-2019). This work was also funded by the EPSRC through grant numbers EP/R00188X/1, EP/W007517/1, and EP/W015137/1. X. Zhang thanks the support from National Natural Science Foundation of China (Grant No. 52130304, 51821002), and Collaborative Innovation Center of Suzhou Nano Science & Technology, Joint International Research Laboratory of Carbon-Based Functional Materials and Devices.

References

- 1 C. Wang, H. Fei, Y. Qiu, Y. Yang, Z. Wei, Y. Tian, Y. Chen and Y. Zhao, Photoinduced birefringence and reversible optical storage in liquid-crystalline azobenzene side-chain polymers, *Appl. Phys. Lett.*, 1999, **74**, 19–21.
- 2 R. Farshchi, M. Ramsteiner, J. Herfort, A. Tahraoui and H. T. Grah, Optical communication of spin information between light emitting diodes, *Appl. Phys. Lett.*, 2011, **98**, 162508.
- 3 Z.-L. Gong, X. Zhu, Z. Zhou, S.-W. Zhang, D. Yang, B. Zhao, Y.-P. Zhang, J. Deng, Y. Cheng, Y.-X. Zheng, S.-Q. Zang, H. Kuang, P. Duan, M. Yuan, C.-F. Chen, Y. S. Zhao, Y.-W. Zhong, B. Z. Tang and M. Liu, Frontiers in circularly polarized luminescence: molecular design, self-assembly, nanomaterials, and applications, *Sci. China: Chem.*, 2021, **64**, 2060–2104.
- 4 J. Crassous, M. J. Fuchter, D. E. Freedman, N. A. Kotov, J. Moon, M. C. Beard and S. Feldmann, Materials for chiral light control, *Nat. Rev. Mater.*, 2023, **8**, 365–371.
- 5 C. W. Tang and S. A. VanSlyke, Organic electroluminescent diodes, *Appl. Phys. Lett.*, 1987, **51**, 913–915.
- 6 L. Frédéric, A. Desmarchelier, L. Favereau and G. Pieters, Designs and Applications of Circularly Polarized Thermally Activated Delayed Fluorescence Molecules, *Adv. Funct. Mater.*, 2021, **31**, 2010281.
- 7 F. Furlan, J. M. Moreno-Naranjo, N. Gasparini, S. Feldmann, J. Wade and M. J. Fuchter, Chiral materials and mechanisms for circularly polarized light-emitting diodes, *Nat. Photonics*, 2024, **18**, 658–668.
- 8 E. Peeters, M. P. Christiaans, R. A. Janssen, H. F. Schoo, H. P. Dekkers and E. Meijer, Circularly polarized electroluminescence from a polymer light-emitting diode, *J. Am. Chem. Soc.*, 1997, **119**, 9909–9910.
- 9 J. L. Greenfield, J. Wade, J. R. Brandt, X. Shi, T. J. Penfold and M. J. Fuchter, Pathways to increase the dissymmetry in the interaction of chiral light and chiral molecules, *Chem. Sci.*, 2021, **12**, 8589–8602.
- 10 H. Uoyama, K. Goushi, K. Shizu, H. Nomura and C. Adachi, Highly Efficient Organic Light-Emitting Diodes from Delayed Fluorescence, *Nature*, 2012, **492**, 234–238.
- 11 Q. Zhang, J. Li, K. Shizu, S. Huang, S. Hirata, H. Miyazaki and C. Adachi, Design of Efficient Thermally Activated Delayed Fluorescence Materials for Pure Blue Organic Light Emitting Diodes, *J. Am. Chem. Soc.*, 2012, **134**, 14706–14709.
- 12 H. Hirai, K. Nakajima, S. Nakatsuka, K. Shiren, J. Ni, S. Nomura, T. Ikuta and T. Hatakeyama, One-Step Borylation of 1,3-Diaryloxybenzenes Towards Efficient Materials for Organic Light-Emitting Diodes, *Angew. Chem., Int. Ed.*, 2015, **54**, 13581–13585.
- 13 T. Hatakeyama, K. Shiren, K. Nakajima, S. Nomura, S. Nakatsuka, K. Kinoshita, J. Ni, Y. Ono and T. Ikuta, Ultrapure blue thermally activated delayed fluorescence molecules: efficient HOMO–LUMO separation by the multiple resonance effect, *Adv. Mater.*, 2016, **28**, 2777–2871.
- 14 H. J. Kim and T. Yasuda, Narrowband Emissive Thermally Activated Delayed Fluorescence Materials, *Adv. Opt. Mater.*, 2022, **10**, 2201714.
- 15 K. R. Naveen, P. Palanisamy, M. Y. Chae and J. H. Kwon, Multiresonant TADF materials: triggering the reverse intersystem crossing to alleviate the efficiency roll-off in OLEDs, *Chem. Commun.*, 2023, **59**, 3685–3702.
- 16 M. Li and C.-F. Chen, Advances in circularly polarized electroluminescence based on chiral TADF-active materials, *Org. Chem. Front.*, 2022, **9**, 6441–6452.
- 17 Y. Xu, Q. Wang, X. Cai, C. Li and Y. Wang, Highly Efficient Electroluminescence from Narrowband Green Circularly Polarized Multiple Resonance Thermally Activated Delayed Fluorescence Enantiomers, *Adv. Mater.*, 2021, **33**, 2100652.
- 18 L. Yuan, Y.-P. Zhang and Y.-X. Zheng, Chiral thermally activated delayed fluorescence materials for circularly polarized organic light-emitting diodes, *Sci. China: Chem.*, 2024, **67**, 1097–1116.
- 19 Y. Xu, Q. Wang, X. Song, Y. Wang and C. Li, New Fields, New Opportunities and New Challenges: Circularly Polarized Multiple Resonance Thermally Activated Delayed Fluorescence Materials, *Chem.–Eur. J.*, 2023, **29**, e202203414.
- 20 L. Poulard, S. Kasemthaveechok, M. Coehlo, R. A. Kumar, L. Frederic, P. Sumsalee, T. d'Anfray, S. Wu, J. Wang,



- T. Matulaitis, J. Crassous, E. Zysman-Colman, L. Favereau and G. Pieters, Circularly polarized-thermally activated delayed fluorescent materials based on chiral bicarbazole donors, *Chem. Commun.*, 2022, **58**, 6554–6557.
- 21 Y. Yang, N. Li, J. Miao, X. Cao, A. Ying, K. Pan, X. Lv, F. Ni, Z. Huang, S. Gong and C. Yang, Chiral Multi-Resonance TADF Emitters Exhibiting Narrowband Circularly Polarized Electroluminescence with an EQE of 37.2, *Angew. Chem., Int. Ed.*, 2022, **61**, e202202227.
 - 22 X. F. Luo, S. Q. Song, X. Wu, C. F. Yip, S. Cai and Y. X. Zheng, A chiral spirofluorene-embedded multiple-resonance thermally activated delayed fluorescence emitter for efficient pure-green circularly polarized electroluminescence, *Aggregate*, 2023, **5**, e445.
 - 23 S.-Q. Song, X. Han, Z.-Z. Huo, C.-F. Yip, X.-F. Hong, M.-N. Ding and Y.-X. Zheng, Chiral multiple-resonance thermally activated delayed fluorescence materials based on chiral spiro-axis skeleton for efficient circularly polarized electroluminescence, *Sci. China: Chem.*, 2024, **67**, 2257–2264.
 - 24 Y. Wang, Z. Y. Lv, Z. X. Chen, S. Xing, Z. Z. Huo, X. F. Hong, L. Yuan, W. Li and Y. X. Zheng, Multiple-resonance thermally activated delayed fluorescence materials based on phosphorus central chirality for efficient circularly polarized electroluminescence, *Mater. Horiz.*, 2024, DOI: [10.1039/d4mh00605d](https://doi.org/10.1039/d4mh00605d).
 - 25 Z. P. Yan, L. Yuan, Y. Zhang, M. X. Mao, X. J. Liao, H. X. Ni, Z. H. Wang, Z. An, Y. X. Zheng and J. L. Zuo, A Chiral Dual-Core Organoboron Structure Realizes Dual-Channel Enhanced Ultrapure Blue Emission and Highly Efficient Circularly Polarized Electroluminescence, *Adv. Mater.*, 2022, **34**, 2204253.
 - 26 L. Yuan, Y. F. Yang, Z. P. Yan, J. J. Hu, D. Mao, H. X. Ni and Y. X. Zheng, Circularly Polarized Electroluminescence from Intrinsically Axial Chiral Materials Based on Bidibenzo[b,d]furan/bidibenzo[b,d]thiophene, *Adv. Funct. Mater.*, 2024, 2403803.
 - 27 L. Yuan, J. W. Xu, Z. P. Yan, Y. F. Yang, D. Mao, J. J. Hu, H. X. Ni, C. H. Li, J. L. Zuo and Y. X. Zheng, Tetraborated Intrinsically Axial Chiral Multi-resonance Thermally Activated Delayed Fluorescence Materials, *Angew. Chem., Int. Ed.*, 2024, **63**, e202407277.
 - 28 S. Xing, X. S. Zhong, X. J. Liao, Y. Wang, L. Yuan, H. X. Ni and Y. X. Zheng, Axially Chiral Multiple Resonance Thermally Activated Delayed Fluorescence Enantiomers for Efficient Circularly Polarized Electroluminescence, *Adv. Opt. Mater.*, 2024, **12**, 2400685.
 - 29 X. J. Liao, D. Pu, L. Yuan, J. Tong, S. Xing, Z. L. Tu, J. L. Zuo, W. H. Zheng and Y. X. Zheng, Planar Chiral Multiple Resonance Thermally Activated Delayed Fluorescence Materials for Efficient Circularly Polarized Electroluminescence, *Angew. Chem., Int. Ed.*, 2023, **62**, e202217045.
 - 30 Y. Xu, H. Hafeez, J. Seibert, S. Wu, J. S. O. Ortiz, J. Crassous, S. Bräse, I. D. W. Samuel and E. Zysman-Colman, [2.2] Paracyclophane-Substituted Chiral Multiresonant Thermally Activated Delayed Fluorescence Emitters for Efficient Organic Light-Emitting Diodes, *Adv. Funct. Mater.*, 2024, 2402036.
 - 31 Y. Zhang, D. Zhang, T. Huang, A. J. Gillett, Y. Liu, D. Hu, L. Cui, Z. Bin, G. Li, J. Wei and L. Duan, Multi-Resonance Deep-Red Emitters with Shallow Potential-Energy Surfaces to Surpass Energy-Gap Law, *Angew. Chem., Int. Ed.*, 2021, **60**, 20498–20503.
 - 32 J. K. Li, X. Y. Chen, Y. L. Guo, X. C. Wang, A. C. Sue, X. Y. Cao and X. Y. Wang, B,N-Embedded Double Hetero[7]helicenes with Strong Chiroptical Responses in the Visible Light Region, *J. Am. Chem. Soc.*, 2021, **143**, 17958–17963.
 - 33 X. Wu, J. W. Huang, B. K. Su, S. Wang, L. Yuan, W. Q. Zheng, H. Zhang, Y. X. Zheng, W. Zhu and P. T. Chou, Fabrication of Circularly Polarized MR-TADF Emitters with Asymmetrical Peripheral-Lock Enhancing Helical B/N-Doped Nanographenes, *Adv. Mater.*, 2022, **34**, 2105080.
 - 34 W. Yang, N. Li, J. Miao, L. Zhan, S. Gong, Z. Huang and C. Yang, Simple Double Hetero[5]helicenes Realize Highly Efficient and Narrowband Circularly Polarized Organic Light-Emitting Diodes, *CCS Chem.*, 2022, **4**, 3463–3471.
 - 35 Z. Ye, H. Wu, Y. Xu, T. Hua, G. Chen, Z. Chen, X. Yin, M. Huang, K. Xu, X. Song, Z. Huang, X. Lv, J. Miao, X. Cao and C. Yang, Deep-Blue Narrowband Hetero[6]helicenes Showing Circularly Polarized Thermally Activated Delayed Fluorescence Toward High-Performance OLEDs, *Adv. Mater.*, 2024, **36**, 2308314.
 - 36 S. Y. Yang, S. N. Zou, F. C. Kong, X. J. Liao, Y. K. Qu, Z. Q. Feng, Y. X. Zheng, Z. Q. Jiang and L. S. Liao, A narrowband blue circularly polarized thermally activated delayed fluorescence emitter with a hetero-helicene structure, *Chem. Commun.*, 2021, 57, 11041–11044.
 - 37 S.-Y. Yang, Q.-S. Tian, X.-J. Liao, Z.-G. Wu, W.-S. Shen, Y.-J. Yu, Z.-Q. Feng, Y.-X. Zheng, Z.-Q. Jiang and L.-S. Liao, Efficient circularly polarized thermally activated delayed fluorescence hetero-[4]helicene with carbonyl-/sulfone-bridged triarylamine structures, *J. Mater. Chem. C*, 2022, **10**, 4393–4401.
 - 38 J. M. dos Santos, D. Sun, J. M. Moreno-Naranjo, D. Hall, F. Zinna, S. T. J. Ryan, W. Shi, T. Matulaitis, D. B. Cordes, A. M. Z. Slawin, D. Beljonne, S. L. Warriner, Y. Olivier, M. J. Fuchter and E. Zysman-Colman, An S-Shaped Double Helicene Showing both Multi-Resonance Thermally Activated Delayed Fluorescence and Circularly Polarized Luminescence, *J. Mater. Chem. C*, 2022, **10**, 4861–4870.
 - 39 Q. Wang, L. Yuan, C. Qu, T. Huang, X. Song, Y. Xu, Y. X. Zheng and Y. Wang, Constructing Highly Efficient Circularly Polarized Multiple-Resonance Thermally Activated Delayed Fluorescence Materials with Intrinsically Helical Chirality, *Adv. Mater.*, 2023, **35**, 2305125.
 - 40 F. Zhang, F. Rauch, A. Swain, T. B. Marder and P. Ravat, Efficient Narrowband Circularly Polarized Light Emitters Based on 1,4-B,N-embedded Rigid Donor-Acceptor Helicenes, *Angew. Chem., Int. Ed.*, 2023, **62**, e202218965.
 - 41 G. Meng, J. Zhou, X. S. Han, W. Zhao, Y. Zhang, M. Li, C. F. Chen, D. Zhang and L. Duan, B-N Covalent Bond Embedded Double Hetero-[n]helicenes for Pure Red



- Narrowband Circularly Polarized Electroluminescence with High Efficiency and Stability, *Adv. Mater.*, 2024, **36**, 2307420.
- 42 W. C. Guo, W. L. Zhao, K. K. Tan, M. Li and C. F. Chen, B,N-Embedded Hetero[9]helicene Toward Highly Efficient Circularly Polarized Electroluminescence, *Angew. Chem., Int. Ed.*, 2024, **63**, e202401835.
 - 43 G. Venugopal, V. Kumar, A. Badrinarayan Jadhav, S. D. Dongre, A. Khan, R. Gonnade, J. Kumar and S. Santhosh Babu, Boron- and Oxygen-Doped pi-Extended Helical Nanographene with Circularly Polarised Thermally Activated Delayed Fluorescence, *Chem.-Eur. J.*, 2024, **30**, e202304169.
 - 44 Y. Xu, Z. Cheng, Z. Li, B. Liang, J. Wang, J. Wei, Z. Zhang and Y. Wang, Molecular-Structure and Device-Configuration Optimizations toward Highly Efficient Green Electroluminescence with Narrowband Emission and High Color Purity, *Adv. Opt. Mater.*, 2020, **8**, 1902142.
 - 45 T. H. Dunning Jr, Gaussian basis sets for use in correlated molecular calculations. I. The atoms boron through neon and hydrogen, *J. Chem. Phys.*, 1989, **90**, 1007–1023.
 - 46 C. Adamo and V. Barone, Toward reliable density functional methods without adjustable parameters: the PBE0 model, *J. Chem. Phys.*, 1999, **110**, 6158–6170.
 - 47 A. Pershin, D. Hall, V. Lemaure, J. C. Sancho-Garcia, L. Muccioli, E. Zysman-Colman, D. Beljonne and Y. Olivier, Highly emissive excitons with reduced exchange energy in thermally activated delayed fluorescent molecules, *Nat. Commun.*, 2019, **10**, 597.
 - 48 D. Hall, J. C. Sancho-Garcia, A. Pershin, G. Ricci, D. Beljonne, E. Zysman-Colman and Y. Olivier, Modeling of Multiresonant Thermally Activated Delayed Fluorescence Emitters - Properly Accounting for Electron Correlation Is Key, *J. Chem. Theory Comput.*, 2022, **18**, 4903–4918.
 - 49 X. Cao, K. Pan, J. Miao, X. Lv, Z. Huang, F. Ni, X. Yin, Y. Wei and C. Yang, Manipulating Exciton Dynamics toward Simultaneous High-Efficiency Narrowband Electroluminescence and Photon Upconversion by a Selenium-Incorporated Multiresonance Delayed Fluorescence Emitter, *J. Am. Chem. Soc.*, 2022, **144**, 22976–22984.
 - 50 I. S. Park, H. Min and T. Yasuda, Ultrafast Triplet-Singlet Exciton Interconversion in Narrowband Blue Organoboron Emitters Doped with Heavy Chalcogens, *Angew. Chem., Int. Ed.*, 2022, **61**, e202205684.
 - 51 I. Kim, K. H. Cho, S. O. Jeon, W. J. Son, D. Kim, Y. M. Rhee, I. Jang, H. Choi and D. S. Kim, Three States Involving Vibronic Resonance is a Key to Enhancing Reverse Intersystem Crossing Dynamics of an Organoboron-Based Ultrapure Blue Emitter, *JACS Au*, 2021, **1**, 987–997.
 - 52 M. K. Etherington, J. Gibson, H. F. Higginbotham, T. J. Penfold and A. P. Monkman, Revealing the spin-vibronic coupling mechanism of thermally activated delayed fluorescence, *Nat. Commun.*, 2016, **7**, 13680.
 - 53 N. G. Connelly and W. E. Geiger, Chemical redox agents for organometallic chemistry, *Chem. Rev.*, 1996, **96**, 877–910.
 - 54 X. Yan, Z. Li, Q. Wang, Y. Qu, Y. Xu and Y. Wang, Achieving highly efficient narrowband sky-blue electroluminescence with alleviated efficiency roll-off by molecular-structure regulation and device-configuration optimization, *J. Mater. Chem. C*, 2022, **10**, 15408–15415.
 - 55 T. Fan, Y. Zhang, D. Zhang and L. Duan, Decoration Strategy in Para Boron Position: An Effective Way to Achieve Ideal Multi-Resonance Emitters, *Chem.-Eur. J.*, 2022, **28**, e202104624.
 - 56 S. Wu, W. Li, K. Yoshida, D. Hall, S. Madayanad Suresh, T. Sayner, J. Gong, D. Beljonne, Y. Olivier, I. D. W. Samuel and E. Zysman-Colman, Excited-State Modulation in Donor-Substituted Multiresonant Thermally Activated Delayed Fluorescence Emitters, *ACS Appl. Mater. Interfaces*, 2022, **14**, 22341–22352.
 - 57 X. Wu, B.-K. Su, D.-G. Chen, D. Liu, C.-C. Wu, Z.-X. Huang, T.-C. Lin, C.-H. Wu, M. Zhu, E. Y. Li, W.-Y. Hung, W. Zhu and P.-T. Chou, The role of host-guest interactions in organic emitters employing MR-TADF, *Nat. Photonics*, 2021, **15**, 780–786.
 - 58 L.-S. Cui, S.-B. Ruan, F. Bencheikh, R. Nagata, L. Zhang, K. Inada, H. Nakanotani, L.-S. Liao and C. Adachi, Long-lived efficient delayed fluorescence organic light-emitting diodes using n-type hosts, *Nat. Commun.*, 2017, **8**, 2250.
 - 59 L. Arrico, L. Di Bari and F. Zinna, Quantifying the Overall Efficiency of Circularly Polarized Emitters, *Chem.-Eur. J.*, 2021, **27**, 2920–2934.
 - 60 D. Zhang, M. Cai, Y. Zhang, D. Zhang and L. Duan, Sterically shielded blue thermally activated delayed fluorescence emitters with improved efficiency and stability, *Mater. Horiz.*, 2016, **3**, 145–151.
 - 61 K. Zhang, X. Wang, Y. Chang, Y. Wu, S. Wang and L. Wang, Carbazole-Decorated Organoboron Emitters with Low-Lying HOMO Levels for Solution-Processed Narrowband Blue Hyperfluorescence OLED Devices, *Angew. Chem., Int. Ed.*, 2023, **62**, e202313084.
 - 62 T. Baumann, M. Budzynski and C. Kasparek, 33-3: TADF Emitter Selection for Deep-Blue Hyper-Fluorescent OLEDs, *SID Int. Symp. Dig. Tech. Pap.*, 2019, **50**, 466–469.

